

Probing molecular chirality on a sub-femtosecond timescale

R. Cireasa^{1,2}, A. E. Boguslavskiy^{3,4,5}, B. Pons⁶, M. C. H. Wong³, D. Descamps⁶, S. Petit⁶, H. Ruf⁶, N. Thiré^{1,7}, A. Ferré⁶, J. Suarez⁸, J. Higuete⁶, B. E. Schmidt⁷, A. F. Alharbi^{3,9}, F. Légaré⁷, V. Blanchet^{1,6}, B. Fabre⁶, S. Patchkovskii^{4,10}, O. Smirnova^{10*}, Y. Mairesse^{6*} and V. R. Bhardwaj^{3*}

Chiral molecules that are non-superimposable mirror images of each other, known as enantiomers, have identical chemical and physical properties unless they interact with another chiral entity, such as chiral light. Chiroptical¹ effects arising from such interactions are used to detect enantiomers in mixtures and to induce enantioselective synthesis and catalysis. Chiroptical effects often arise from the interplay between light-induced electric- and magnetic-dipole transitions in a molecule and evolve on ultrafast electronic timescales. Here we use high-harmonic generation^{2,3} from a randomly oriented gas of molecules subjected to an intense laser field, to probe chiral interactions on these sub-femtosecond timescales. We show that a slight disparity in the laser-driven electron dynamics in the two enantiomers is recorded and amplified by several orders of magnitude in the harmonic spectra. Our work shows that chiroptical detection can go beyond detecting chiral structure^{4–7} to resolving and controlling chiral dynamics on electronic timescales.

The high-harmonic generation (HHG) process, which we use to induce and monitor chiral dynamics, occurs when an intense femtosecond laser pulse is focused in a gaseous medium^{2,3}. It is an extreme nonlinear frequency conversion process, which can be understood semi-classically as a sequence of three steps^{3,8}: ionization in a strong infrared (IR) field, laser-induced acceleration of the liberated electron, and its recombination with the parent ion, all within one laser cycle. Recombination results in emission of coherent radiation extending from the vacuum ultraviolet to the soft X-ray region⁹. Crucially, the radiation spectrum records a movie of the recombining system, with each harmonic representing a single frame¹⁰. The time resolution—the interval between the frames—is determined by the difference in the emission times between the consecutive harmonics. In the conditions of our experiment it is $\Delta t \sim 0.1$ fs (ref. 11), determined by the laser wavelength and intensity used. Capitalizing on this property of high-harmonic emission, we introduce an ultrafast enantiosensitive spectroscopic probe, chiral HHG (cHHG), measuring the HHG yields from enantiomers interacting with an intense, elliptically polarized infrared laser field as a function of ellipticity.

Chiroptical discrimination¹ in rotationally isotropic media usually relies on the difference in absorption (circular dichroism, CD), refraction, intensity of Raman scattering (Raman optical activity),

or the low-order nonlinear response¹² of two enantiomers to circularly polarized light. In conventional chiroptical spectroscopy the chiral response often arises on the sub-femtosecond, electronic, timescale from the interplay between the electric- and magnetic-dipole transitions, but is monitored on an orders of magnitude longer timescale¹³. cHHG is the first ultrafast all-optical non-resonant detection scheme, where the electronic chiral response can be monitored on the sub-femtosecond timescale. In contrast to most CD-type techniques, cHHG benefits from longer wavelength (mid-IR) laser fields and does not require resonant excitations, cold molecular samples and/or long acquisition times. The underlying principle is general and applicable to a large variety of molecules. We examine two benchmark systems: epoxypropane (C_3H_6O) and fenchone ($C_{10}H_{16}O$), both previously explored by optical rotation^{14,15} and photoelectron CD methods (PECD; refs 16–22).

The measured dependence of HHG yield on ellipticity ϵ of the $\sim 1,800$ nm driving laser is shown in Fig. 1a,b (epoxypropane) and Supplementary Fig. 1 (fenchone). The use of mid-IR light is essential for obtaining extended HHG spectra from molecules with modest ionization potentials $I_p \leq 10$ eV (ref. 23). In achiral species, the HHG yield is a symmetric Gaussian function of ϵ (ref. 24), with its maximum at $\epsilon = 0$. It decays quickly as ϵ increases: in an elliptical driving field, the liberated electron acquires a lateral drift, which increases with ϵ . At $\epsilon \geq 20\%$, the laser-driven electron misses the parent molecule, quenching electron–hole recombination and HHG. In contrast, in a randomly oriented gas of chiral molecules we find the HHG yield to be asymmetric, with its maximum at a small non-zero ϵ_0 . The cHHG exhibits elliptical dichroism.

The maximizing ellipticities $\epsilon_0(N)$ as a function of harmonic order N are shown in Fig. 2a (epoxypropane) and b (fenchone). The measured ϵ_0 values reach ± 1 –2% (here and below the opposite signs of ϵ denote opposite field helicity). The dependence $\epsilon_0(N)$ is essentially flat for fenchone. In epoxypropane, $\epsilon_0(N)$ increases from zero to 1% around 28 eV (harmonic 41), falls to zero around 43 eV (harmonic 63), and again deviates slightly from zero for significantly higher harmonics. At least in the 24–35 eV range, the measured ϵ_0 in fenchone is insensitive to laser intensity.

High-harmonic generation is typically treated within the dipole approximation, which neglects the magnetic component of the laser field and the spatial dependence of the electric field. This

¹LCAR, Université de Toulouse, 31062, Toulouse Cedex 09, France. ²Institut des Sciences Moléculaires d'Orsay, Université Paris Sud, 91405 Orsay Cedex, France. ³University of Ottawa, 150 Louis Pasteur, Ottawa, K1N 6N5, Canada. ⁴NRC Canada, 100 Sussex Drive, Ottawa, K1A 0R6, Canada. ⁵Department of Physics, Queen's University, 99 University Avenue, Kingston, Ontario K7L 3N6, Canada. ⁶CElia, Université de Bordeaux - CNRS - CEA, F33405 Talence, France. ⁷INRS-EMT, Advanced Laser Light Source, 1650 Lionel-Boulet Blvd, Varennes, J3X1S2, Canada. ⁸Departamento de Química, Universidad Autónoma de Madrid, E-28049 Madrid, Spain. ⁹King Abdulaziz City for Science and Technology (KACST), PO Box 6086, Riyadh 11442, Saudi Arabia. ¹⁰Max Born Institute for Nonlinear Optics and Short Pulse Spectroscopy, Max-Born-Straße 2A, 12489 Berlin, Germany. *e-mail: olga.smirnova@mbi-berlin.de; mairesse@celia.u-bordeaux1.fr; ravi.bhardwaj@uottawa.ca

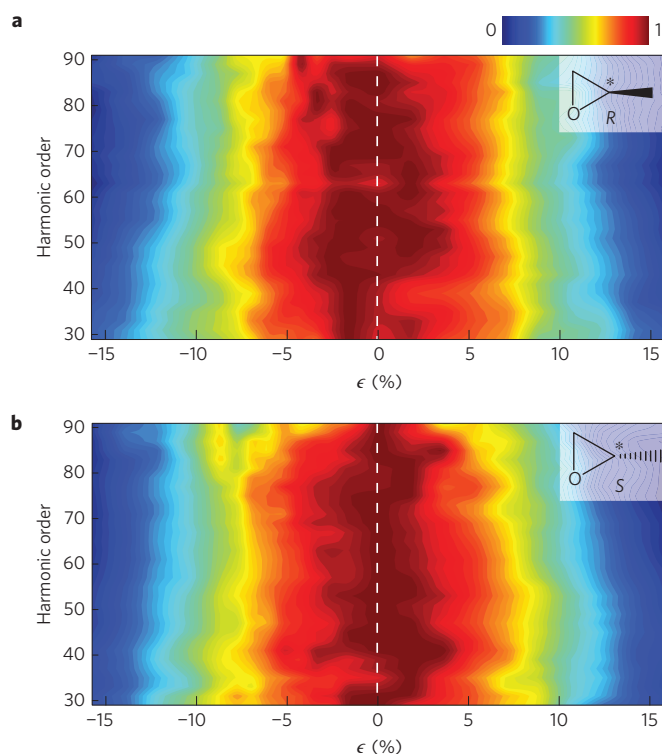


Figure 1 | Ellipticity dependence of HHG yield in epoxypropane.

a,b, High-harmonic yield as a function of laser ellipticity for the (R)- and (S)-enantiomers of epoxypropane, respectively (schematically in the inset); epoxypropane contains one stereogenic centre, indicated by an asterisk. Measurements are taken using radiation at 1,770 nm, with intensity $\sim 5 \times 10^{13} \text{ W cm}^{-2}$. For every harmonic the ellipticity-dependent yield is normalized to the maximum yield, with no further data processing.

approximation is justified by the difference between the laser wavelength ($\sim 1 \mu\text{m}$) and the typical size of a molecule ($\sim 1 \text{ nm}$). However, in the dipole approximation the chiral dichroism in high-harmonic emission is absent for randomly oriented molecules. Indeed, consider a randomly oriented ensemble of ‘right-handed’ (R) molecules. Reflecting this ensemble in the field polarization plane gives an ensemble of left-handed (S) molecules. However, the laser electric field (a polar vector) remains unchanged on this reflection. Thus, the spectrum of the nonlinear response to the electric field vector will be the same for R- and S-ensembles (see Supplementary Information).

In contrast, the laser magnetic field changes direction on reflection in the polarization plane, making the microscopic interaction chiral. During harmonic generation, the magnetic field can interact with both the transiently liberated electron and the hole left behind (that is, with the residual ionic core), leading to two possible mechanisms of cHHG (Fig. 3).

In the type-I mechanism, the laser magnetic field acts on the liberated electron. The Lorentz force pushes the electron out of the polarization plane, and in an elliptically polarized field the electron trajectory between ionization and recombination becomes chiral. Recombination with the chiral parent ion then leads to chiral discrimination (Fig. 3 and Supplementary Information).

In the type-II mechanism, the laser magnetic field acts on the parent ion, inducing transitions between the cation states. The weak component of the elliptical field is always aligned with the major axis of the magnetic field, controlling the interplay of the electric-dipole and the magnetic-dipole²⁵ transitions along this direction. This process is chiral—it is sensitive to the sign of the magnetic dipole, which is opposite in the two enantiomers. Thus,

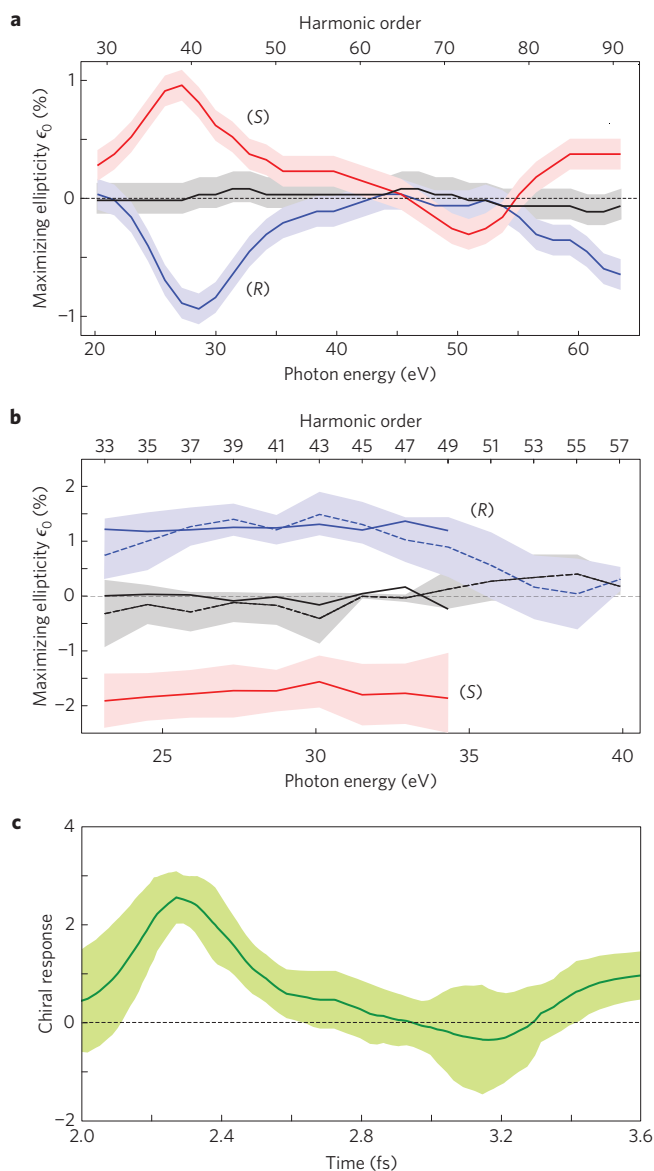


Figure 2 | Measured ellipticity dependence of HHG and time-resolved chiral response. For each harmonic order, the corresponding ellipticity dependence is fitted with a Gaussian function, the central position of which we call a maximizing ellipticity ϵ_0 . **a,b**, ϵ_0 as functions of the harmonic order (top axis) and the emission energy (bottom axis) for epoxypropane (**a**) and fenchone (**b**). Red and blue traces correspond to enantiomers of epoxypropane (**a**) or fenchone (**b**) (the latter is acquired at 1,850 nm, $3.0 \times 10^{13} \text{ W cm}^{-2}$ (solid) and $3.5 \times 10^{13} \text{ W cm}^{-2}$ (dashed lines)). A simultaneous change of the sign of ellipticity and the enantiomer leaves the measured HHG spectrum unchanged within the experimental error. The grey line shows the non-chiral reference (xenon in **a**, ethanol in **b**). The absolute sign of ellipticity is undetermined. Raw data for fenchone and details of data analysis are given in Supplementary Information. **c**, Ellipticity-weighted time-resolved chiral response for epoxypropane $S(N) = \tilde{S}(N, \epsilon)/\epsilon$, reconstructed from the experimental data (see equation (1) and Methods). The experimental errors are the standard deviation, and are shown as shaded areas surrounding the solid lines.

it is affected by the sign of the helicity. Driven by the strong laser field, the attosecond hole dynamics²⁶ between ionization and recombination become enantiomer-sensitive. This dependence makes electron–hole recombination and the associated harmonic emission chiral-sensitive.

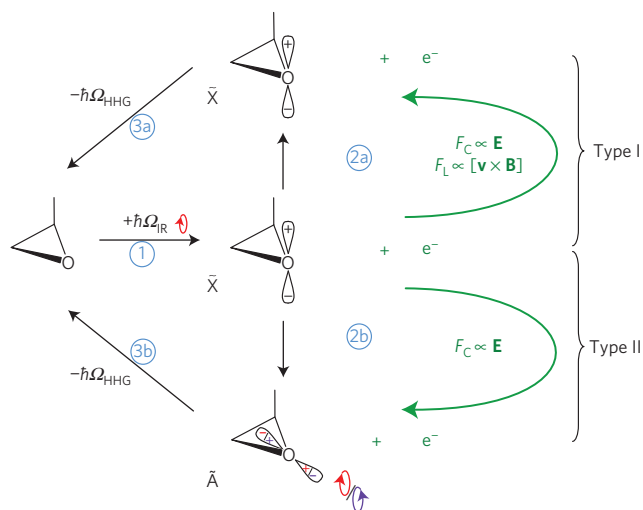


Figure 3 | Mechanisms of chiral sensitivity for high-harmonic emission.

Type I: (1) Tunnel ionization of a neutral molecule produces an electron e^- and a molecular cation in its ground state (\tilde{X}); (2a) The electron is accelerated by the laser electric field (\mathbf{E}) and acquires chiral displacement due to the action of the Lorentz force ($\mathbf{v} \times \mathbf{B}$); (3a) The electron recombines with the ion, emitting an energetic photon ($\hbar\Omega_{\text{HHG}}$). Type II: (2b) The ion undergoes sub-cycle electric- and magnetic-dipole transitions, which change the ionic state (for example, $\tilde{X} \rightarrow \tilde{A}$) between ionization and recombination and open chiral-sensitive HHG channels XA and AX; (3b) Recombination leads to emission of an XUV photon. The interference between the chiral-sensitive HHG channels XA and AX and the non-chiral HHG channels XX and AA associated with ionization and recombination to the same orbital leads to homodyne enhancement of the chiral signal.

Both mechanisms are general. The calculations (see Supplementary Information) show that the type-I chiral asymmetry is one to two orders of magnitude below the experimentally observed values. At non-relativistic field intensities, the Lorentz force is too weak to displace the liberated electronic wavepacket during the ~ 3 fs interval between ionization and recombination. The typical $\sim 10^{-2}$ – 10^{-1} Bohr displacement of the electronic wavepacket is too small compared to its own extension and the molecule size.

The type-II mechanism, caused by chiral-sensitive transitions in the ion, corresponds to ionization from one orbital and recombination to another orbital. It requires the laser field to move the hole between orbitals on a sub-laser-cycle timescale. The strength of the chiral-sensitive sub-cycle transitions depends on the electronic structure of the molecule. We find that epoxypropane and fenchone represent two limiting cases. In epoxypropane the chiral-sensitive transitions are weak, in fenchone they are strong, but the overall harmonic signal is chiral in both molecules. The type-II mechanism is consistent with our experiment.

The extreme sensitivity of the maximizing ellipticity $\epsilon_0(N)$ to harmonic order in epoxypropane (Fig. 2a) reveals the imprint of the sub-cycle hole dynamics on the chiral response. In epoxypropane, the ground state of the cation (\tilde{X}) corresponds to the removal of the lone pair electron from the out-of-plane p orbital of the oxygen atom. The first excited state (\tilde{A}), located 0.9 eV (ref. 27) above \tilde{X} , corresponds to electron removal from another oxygen lone pair, stabilized by partial involvement in the C–O bonds. Ionization in a strong laser field produces both states with equal efficiency (see Supplementary Information), opening two main HHG channels, denoted as ‘XX’ and ‘AA’. In this notation the first letter identifies the ionization channel, while the second letter shows the recombination channel: for example, ‘XX’ implies ionization into the ionic state \tilde{X} and recombination of the liberated electron with the same state. These ‘direct’ channels do not involve any magnetic-dipole

transitions in the ion, and therefore carry no chiral signal. However, laser-induced transitions in the ion between ionization and recombination open two additional ‘cross-channels’²⁶, ‘XA’ and ‘AX’. For example, the ‘AX’ channel corresponds to ionization into the \tilde{A} state but recombination into the \tilde{X} state, enabled by the $\tilde{A} \rightarrow \tilde{X}$ transition in the cation between ionization and recombination. The cross-channels involve magnetic-dipole transitions and are thus inherently enantioselective. To evaluate their relative strengths, we look at the laser-induced transitions in the ion, shown in Fig. 4a–d for the two epoxypropane enantiomers, as a function of ellipticity and the harmonic number. We can make three key observations.

First, owing to the magnetic-dipole coupling, the laser-induced transitions are chiral. Their probability is sensitive to the field helicity and is opposite in two enantiomers. Second, the signal from the cross-channels is about 10^{-3} of the signal from the direct channels, owing to the weak dipole coupling between the states \tilde{X} and \tilde{A} . Third, the signal increases with the harmonic number, reflecting the increasing time delay between ionization and recombination, and thus the increasing time for the chiral-sensitive transitions.

The last two observations do not yet explain the observed sharp peak in the chiral response at harmonic 41 in epoxypropane. The missing piece of the puzzle reveals itself once we recall that the hole dynamics between ionization and recombination leads to accumulation of the phase between the high-harmonic channels and can result in destructive interference between the main channels XX and AA (ref. 28). In epoxypropane, this happens at harmonic 41, leading to strong suppression of the non-chiral signal at the single-molecule level, and the relative enhancement of the chiral signal. Model calculations shown in Fig. 4e,f agree with the experiment (see Supplementary Information).

In fenchone the situation is different. The dense spectrum of electronically excited states in the fenchone cation²⁰ and large dipoles associated with several states lead to strong sub-cycle transitions and to a substantial population transfer between ionic states (see Supplementary Information). The signal from chiral-sensitive cross-channels is comparable to that from the direct channels. Destructive interference between specific channels is not needed to reveal the chiral signal. The interference between these chiral-sensitive HHG channels and the non-chiral HHG channels associated with ionization and recombination to the same orbital leads to homodyne enhancement of the chiral signal. We expect that this picture will be characteristic for large polyatomic molecules with strong permanent and transition dipoles.

We now use the experimental data to reconstruct the time-dependent chiral response. The chiral signal is $\tilde{S}(N, \epsilon) = 2[Y_S(N, \epsilon) - Y_R(N, \epsilon)]/[Y_S(N, \epsilon) + Y_R(N, \epsilon)]$, where $Y_{S,R}(N, \epsilon)$ are the yields of harmonic N for S - and R -enantiomers. In the Supplementary Information we show that, for small ϵ , on the one hand

$$\tilde{S}(N, \epsilon) \simeq 2 \frac{\epsilon \epsilon_0(N)}{\sigma^2} \quad (1)$$

and on the other hand

$$\tilde{S}(N, \epsilon) \simeq 4\epsilon \frac{|\delta D_{\text{ch}}(N)|}{|D^{(0)}(N)|} \cos \Phi_{\text{ch}}(N) \quad (2)$$

Here $D^{(0)}(N)$ is the complex-valued harmonic amplitude, which is not chiral-sensitive, $\epsilon \delta D_{\text{ch}}(N)$ is its chiral-sensitive counterpart, which has opposite sign for S - and R -molecules; for small ϵ it scales linearly with ϵ . $\Phi_{\text{ch}}(N)$ is the relative phase between the chiral and achiral emission amplitudes. The ellipticity $\epsilon_0(N)$ maximizes the ϵ -dependent harmonic signal, and σ is the measured width of the overall Gaussian dependence of the harmonic yield on laser ellipticity (see Supplementary Information).

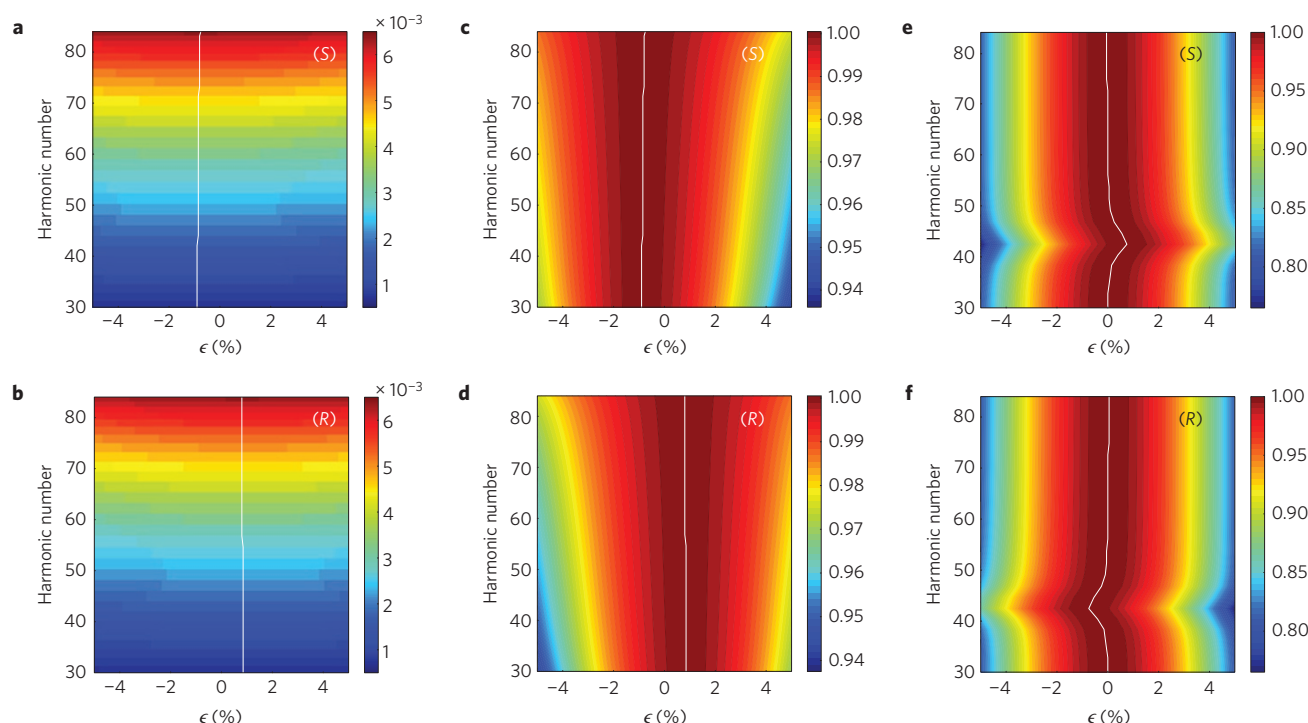


Figure 4 | The origin of chiral sensitivity of high-harmonic emission in epoxypropane. **a,b**, Probabilities of laser-induced transitions ${}^2\tilde{X} \leftarrow {}^2\tilde{A}$ in the transient ion versus laser ellipticity, calculated for each harmonic order N between the time of ionization $t_i(N)$ and the time of recombination $t_r(N)$, corresponding to this harmonic order N . The S-enantiomer (**a**) and R-enantiomer (**b**) show opposite response to the sign of the ellipticity. The small difference in the response of the two enantiomers is marked by the white line corresponding to the maximal signal. This line is offset from zero in opposite directions for the two enantiomers. **c,d**, The same as in **a,b**, but normalized to the maximum of the transition probability versus ellipticity for each harmonic. **e,f**, Calculations of the ellipticity dependence of the high-harmonic signal in S-epoxypropane (**e**) and R-epoxypropane (**f**) confirm that the chiral-sensitive signal is particularly strong around harmonics 41–43, where the main (chiral-insensitive) high-harmonic channels XX and AA interfere destructively. For each harmonic the signal is normalized to its maximum as a function of ellipticity in the same way as in Fig. 1. Details of the calculations are given in the Methods and Supplementary Information.

Normalizing $\tilde{S}(N, \epsilon)$ to ϵ , we obtain an ϵ -independent measure of the cHHG response, $S(N) = \tilde{S}(N, \epsilon)/\epsilon = 2\epsilon_0(N)/\sigma^2 = 4(|\delta D_{\text{ch}}(N)|)/(|D^{(0)}(N)|) \cos \Phi_{\text{ch}}(N)$. Thus, $\epsilon_0(N)$ directly measures the chiral contribution to the harmonic amplitude. Figure 2c shows the time-resolved chiral signal in epoxypropane reconstructed from the experimental measurements of $\epsilon_0(N)$ (Fig. 3a). To convert harmonic number N into time, we used standard time–energy mapping^{10,11}.

Even though disparity in laser-driven hole dynamics in the two enantiomers is only about 2×10^{-4} in probability in epoxypropane (around harmonic 41), both $\tilde{S}(N, \epsilon = \epsilon_0(N))$ and $S(N)$ reach very large values, from a few percent for $\tilde{S}(N)$ to a few hundred percent for $S(N)$, corresponding to several orders of magnitude enhancement. There are several reasons for this amplification. First, the interference of magnetic-dipole and electric-dipole transitions driven by the elliptical field increases the probability of the chiral-sensitive transition to about 10^{-3} . Second, homodyne enhancement in the harmonic light: the chiral contribution is added coherently to the dominant achiral contribution. Thus, $\tilde{S}(N, \epsilon)$ is proportional to the emission amplitude (equation (2)). Third, the high laser intensity makes weak magnetic-dipole transitions efficient. Finally, the steep gradient and universal character of the HHG dependence on the laser ellipticity ϵ allows us to identify even small shifts of the ellipticity dependence between the two enantiomers. For fenchone the experimentally measured elliptical dichroism and the chiral response $\tilde{S}(N, \epsilon) = \epsilon S(N)$ is as high as 10% for $\epsilon = 1\%$, reaching up to 20% for higher ϵ , on par with PECD measurements for fenchone^{20,22} in circularly polarized light. Note that the PECD signal is already present in

the electric-dipole response and does not involve weak magnetic field effects. This comparison highlights the sensitivity of our method and strong enhancement of the weak chiral-sensitive magnetic-dipole transitions.

In our experiments, the chiroptical response is associated with laser-induced multi-electron dynamics in the cation, evolving on the electronic timescale. Although the degree of chirality introduced by the monochromatic plane wave fields in the type-I mechanism is slight, an appropriately shaped driving field²⁹ may yield a high degree of chiral dichroism, and possibly enable selective probing of individual chiral centres within a molecule. In the type-II mechanism, the control of hole dynamics using elliptically polarized multicolour fields, such as the combination of a fundamental field and its second harmonic, can lead to alternative and possibly more sensitive schemes of cHHG detection. It has been shown theoretically that excitation of a ring current in a neutral molecule may lead to the production of highly elliptic harmonic emission³⁰. In a chiral molecule, excitation of such currents may be enantiosensitive, leading to the possibility of mapping molecular chirality on that of the high-harmonic light. Femtosecond-resolved measurements via chiral HHG should provide new insights into the nature of chiral interactions, including both primary electronic dynamics in the light-induced chiral response and the chirality of fundamental biological processes.

Methods

Methods and any associated references are available in the [online version of the paper](#).

Received 3 October 2014; accepted 19 May 2015;
published online 29 June 2015

References

- Berova, N., Polavarapu, P. L., Nakanishi, K. & Woody, R. W. (eds) *Comprehensive Chiroptical Spectroscopy* Vol. 1 (Wiley, 2012).
- Ferray, M. *et al.* Multiple-harmonic conversion of 1064 nm radiation in rare gases. *J. Phys. B* **21**, L31–L35 (1988).
- Corkum, P. B. Plasma perspective on strong field multiphoton ionization. *Phys. Rev. Lett.* **71**, 1994–1997 (1993).
- Herwig, P. *et al.* Imaging the absolute configuration of a chiral epoxide in the gas phase. *Science* **342**, 1084–1086 (2013).
- Jiang, J. *et al.* Observation of possible topological in-gap surface states in the Kondo insulator SmB_6 by photoemission. *Nature Commun.* **4**, 3010 (2013).
- Pitzer, M. *et al.* Direct determination of absolute molecular stereochemistry in gas phase by Coulomb explosion imaging. *Science* **341**, 1096–1100 (2013).
- Patterson, D., Schnell, M. & Doyle, J. M. Enantiomer-specific detection of chiral molecules via microwave spectroscopy. *Nature* **497**, 475–477 (2013).
- Schafer, K. J., Yang, B., DiMauro, L. F. & Kulander, K. C. Above threshold ionization beyond the high harmonic cutoff. *Phys. Rev. Lett.* **70**, 1599–1602 (1993).
- Popmintchev, T. *et al.* Bright coherent ultrahigh harmonics in the keV X-ray regime from mid-infrared femtosecond lasers. *Science* **336**, 1287–1291 (2012).
- Baker, S. *et al.* Probing proton dynamics in molecules on an attosecond time scale. *Science* **312**, 424–427 (2006).
- Doumy, G. *et al.* Attosecond synchronization of high-order harmonics from midinfrared drivers. *Phys. Rev. Lett.* **102**, 093002 (2009).
- Fischer, P. & Hache, F. Nonlinear optical spectroscopy of chiral molecules. *Chirality* **17**, 421–437 (2005).
- Rhee, H. *et al.* Femtosecond characterization of vibrational optical activity of chiral molecules. *Nature* **458**, 310–313 (2009).
- Aberhalden, E. & Eichwald, E. Über optisch-aktives Propylenglykol und optisch-aktive β -Oxy-buttersäure. *Ber. Dtsch. Chem. Ges.* **51**, 1312–1322 (1918).
- Bouchardat, G. & Lafont, J. Synthetical isoborneols; their identity with the fenchylic alcohols. *C. R. Hebd. Seances Acad. Sci.* **126**, 755–757 (1898).
- Turchini, S. *et al.* Circular dichroism in photoelectron spectroscopy of free chiral molecules: Experiment and theory on methyl-oxirane. *Phys. Rev. A* **70**, 014502 (2004).
- Stranges, S. *et al.* Valence photoionization dynamics in circular dichroism of chiral free molecules: The methyl-oxirane. *J. Chem. Phys.* **122**, 244303 (2005).
- Stener, M., Fronzoni, G., Di Tommaso, D. & Decleva, P. Density functional study on the circular dichroism of photoelectron angular distribution from chiral derivatives of oxirane. *J. Chem. Phys.* **120**, 3284–3296 (2004).
- Garcia, G. A., Nahon, L., Daly, S. & Powis, I. Vibrationally induced inversion of photoelectron forward–backward asymmetry in chiral molecule photoionization by circularly polarized light. *Nature Commun.* **4**, 2132 (2013).
- Powis, I., Harding, C. J., Garcia, G. A. & Nahon, L. A valence photoelectron imaging investigation of chiral asymmetry in the photoionization of fenchone and camphor. *ChemPhysChem* **9**, 475–483 (2008).
- Ulrich, V. *et al.* Giant chiral asymmetry in the C 1s core level photoemission from randomly oriented fenchone enantiomers. *J. Phys. Chem. A* **112**, 3544–3549 (2008).
- Lux, C. *et al.* Circular dichroism in the photoelectron angular distributions of camphor and fenchone from multiphoton ionization with femtosecond laser pulses. *Angew. Chem. Int. Ed.* **51**, 5001–5005 (2012).
- Torres, R. *et al.* Extension of high harmonic spectroscopy in molecules by a 1300 nm laser field. *Opt. Express* **18**, 3174–3180 (2010).
- Ivanov, M. Y., Brabec, T. & Burnett, N. Coulomb corrections and polarization effects in high-intensity high-harmonic emission. *Phys. Rev. A* **54**, 742–745 (1996).
- Kroener, D. Chiral distinction by ultrashort laser pulses: Electron wavepacket dynamics incorporating magnetic interactions. *J. Phys. Chem. A* **115**, 14510–14518 (2011).
- Mairesse, Y. *et al.* High harmonic spectroscopy of multichannel dynamics in strong-field ionization. *Phys. Rev. Lett.* **104**, 213601 (2010).
- Kimura, K., Katsumata, S., Achiba, Y., Yamazaki, T. & Iwata, S. *Handbook of He I Photoelectron Spectra of Fundamental Organic Molecules* (Japan Scientific Societies Press, 1981).
- Smirnova, O. *et al.* High harmonic interferometry of multi-electron dynamics in molecules. *Nature* **460**, 972–977 (2009).
- Cundiff, S. T. & Weiner, A. M. Optical arbitrary waveform generation. *Nature Photon.* **4**, 760–766 (2010).
- Xie, X. *et al.* Internal momentum state mapping using high harmonic radiation. *Phys. Rev. Lett.* **101**, 033901 (2008).

Acknowledgements

Experiments on epoxypropane were performed at Advanced Laser Light Source in Montreal. We thank A. Laramée and F. Poitras for their technical expertise. Experiments on fenchone were performed at CELIA, Université de Bordeaux, Talence. We thank E. Constant, E. Cormier and E. Mével for providing key apparatus used in the experiment. We thank M. Y. Ivanov, L. Nahon and M. Spanner for fruitful discussions. We acknowledge financial support from Natural Science and Engineering Research Council of Canada, Canadian Foundation for Innovation, Canada Research Chairs, FRQNT, MDEIE, CIPI, CFI, ANR (ANR-08-JCJC-0029 HarMoDyn), the Conseil Régional d'Aquitaine (20091304003 ATTOMOL and 2.1.3-09010502 COLA2), the European Union (Laserlab), the European COST Action CM1204 XLIC, the EU Marie Curie ITN network CORINE, Grant Agreement No. 264951, and the support of Einstein foundation project A-211-55 Attosecond Electron Dynamics.

Author contributions

R.C. and A.E.B. contributed equally to the experimental work. A.E.B. and V.R.B. designed experiments on epoxypropane and analysed the data; A.E.B., M.C.H.W. and A.F.A., in collaboration with B.E.S., N.T. and F.L., performed experiments on epoxypropane at ALLS. R.C., B.F., A.F., J.H., H.R., N.T., V.B. and Y.M. designed, conducted and analysed the fenchone measurements. D.D. and S.Petit operated the laser system at CELIA. J.S. and B.P. performed the TDSE calculations for the model chiral molecules and analysed the type-I mechanism of cHHG. S.Patchkovskii proposed and analysed the type-I mechanism of cHHG and performed quantum chemical calculations for epoxypropane and fenchone. O.S. proposed and analysed the type-II mechanism of cHHG and the reconstruction of the time-dependent chiral response. All authors contributed to writing the manuscript.

Additional information

Supplementary information is available in the online version of the paper. Reprints and permissions information is available online at www.nature.com/reprints. Correspondence and requests for materials should be addressed to O.S., Y.M. or V.R.B.

Competing financial interests

The authors declare no competing financial interests.

Methods

Epoxypropane measurements at ALLS. Measurements on epoxypropane were performed using a high-energy optical parametric amplifier (OPA) available at Advanced Laser Light Source (ALLS) in Montreal, Canada. The OPA was pumped by 5 mJ, 800 nm, 30 fs pulses from a Ti:sapphire laser operating at 100 Hz, delivering 1.2 mJ of 1,770 nm pulses with a duration of 50 fs, measured by frequency-resolved optical gating. The laser light was then coupled into an evacuated hollow-core capillary (1 m in length and 400 μ m in size) to spatially filter the beam.

High harmonics were generated in a gas cell by focusing 0.6 mJ spatially filtered pulses, after passing through a 3 mm thick CaF₂ window, with a $f = 25$ cm spherical mirror ($f\# = 30$). The gas cell consisted of two concentric cylindrical cells, each having two in-line pinholes of 600 μ m. Gas was delivered to the inner cell through a 1/4-inch Teflon tube connected to a vial with liquid epoxypropane that was temperature stabilized by an ice-water bath. Epoxypropane was obtained from Sigma-Aldrich (purity of 99%). The pressure in the gas cell was monitored with a Baratron gauge. The outer cell was pumped by a 500 l min⁻¹ roughing pump. The gas cell has an effective interaction length of 10 mm and is mounted on an XYZ manipulator to permit precision alignment with respect to the laser axis.

The source and detector chambers were differentially pumped through a tube 3 mm in diameter and 5 cm in length. Different harmonic orders are detected using a grazing-incidence concave grating (1,200 lines mm⁻¹) which disperses and focuses them onto a microchannel plate (MCP) (15 mm \times 75 mm) coupled to a phosphor screen. The screen was imaged with a charge coupled device (CCD) camera. The MCP voltage was adjusted to keep the detection in the linear regime. The harmonic spectra were obtained under optimal phase-matching conditions by adjusting the position of the laser focus with respect to the pinholes and the absolute pressure inside the gas cell. The spectrometer was calibrated by using the Cooper minimum in the HHG spectrum of argon as a reference. This technique was validated in the past by measuring the harmonic spectrum with an aluminium filter inserted in the beam path and comparing it with the calculated transmission spectrum of a known thickness of aluminium.

The polarization state of the incident light was controlled and the ellipticity ϵ (defined as the ratio of the two orthogonal electric fields of the laser light) was varied by a zero-order quarter-wave plate or by rotating a half-wave plate in front of the quarter-wave plate. The latter approach fixed the polarization ellipse in space while the ellipticity was varied. As the angles used in the experiment were small, both methods produced similar results. The waveplates, mounted on a motorized rotation stage (resolution of 0.01°), were rotated in steps of 0.15° close to linear polarization ($\epsilon = 0$) and in larger steps at higher ellipticities ($\epsilon > 0.08$).

The waveplates were calibrated and linear polarization was determined by finding the maximum harmonic signal in xenon. Two successive ellipticity scans were carried out (positive to negative ellipticity and back to positive) and the harmonic signal was averaged to compensate for slow drifts in experimental parameters. Control measurements in xenon were taken before and after the measurements in epoxypropane to get a zero-ellipticity reference and check the stability of the laser parameters during the measurement.

The intensity used in the experiment was 5×10^{13} W cm⁻². The intensity calibration was achieved by monitoring the cutoff harmonics from argon and validated by measuring its saturation intensity using a fast ionization gauge. The ion yield measured by the fast ionization gauge as a function of laser pulse energy was plotted in a semi-log plot. Extrapolation of the linear portion of the ion signal curve defined the saturation energy, and comparison with the calculated ion yield using the ADK model provided the saturation intensity. The yield of every harmonic was extracted from the image at each angle of the waveplate. The resulting data matrix was smoothed both along the harmonic number and the ellipticity dimension.

Fenchone measurements at CELIA. The fenchone measurements were performed using the AUREOLE laser system at CELIA. A high-energy TOPAS system was pumped by 30 fs, 4.7 mJ, 800 nm pulses at 1 kHz, delivering 50 fs 800 μ J pulses at 1,850 nm. The output beam was sent to a motorized zero-order half-wave plate and a fixed zero-order quarter-wave plate to define the laser ellipticity ϵ , and focused by a $f = 37.5$ cm mirror into a 2 mm gas cell connected to an oven. The gas cell was closed by Teflon which was drilled by the laser on both sides of the cell. Enantiopure fenchone (Sigma-Aldrich) was heated to 100 °C, reaching a vapour pressure of 60 mbar. High harmonics were detected using a similar set-up as for the ALLS experiment. The ellipticity dependence of the high-harmonic signal³¹ was measured by performing four consecutive scans of the ellipticity, from negative to positive and back. Calibration measurements of the zero ellipticity were made by generating harmonics in ethanol. The measured dependence of HHG yield on ellipticity is shown in the Supplementary Information (Supplementary Fig. 1).

Sub-cycle dynamics, chiral HHG signals, and maximizing ellipticity. Let $D_{R,S}(N, \epsilon)$ be the amplitudes of harmonic radiation for R and S enantiomers at the frequency $\Omega = N\omega$, for laser ellipticity ϵ . The general relationship between the dipole $D(N)$ associated with high-harmonic emission and the underlying

multi-electron dynamics has been discussed in detail in the literature (see, for example, refs 26,28,32,33). A very good approximation is given by

$$D(N) = \langle \Psi^{(D)}(t_N) | \hat{d} | \Psi^{(c)}(t_N) \rangle \quad (3)$$

Here $\Psi^{(D)}(t)$ is the time-dependent Dyson orbital describing dynamics in the cation, that is, the overlap between the time-dependent, laser-driven $N_c - 1$ electron wavefunction of the cation and the N_c electron wavefunction of the ground electronic state of the neutral, $|\Psi^{(c)}(t)\rangle$ is the wavefunction of the continuum electron, and t_N is the recombination time corresponding to the N th harmonic. This explicit expression is not essential for the general analysis below, but is useful for the physical picture.

In elliptically polarized field, both $|\Psi^{(D)}(t)\rangle$ and $|\Psi^{(c)}(t)\rangle$ are modified compared to the case of linear polarization. First, the continuum wavepacket $|\Psi^{(c)}(t, \epsilon)\rangle$ is displaced in the lateral direction and starts to miss the cation with increasing ϵ , leading to the well-known Gaussian decay of the harmonic amplitude (equation (3)) with ϵ (see, for example, ref. 24) as $\exp(-\epsilon^2/4\sigma^2)$ ($\sigma \simeq 0.085$ for our experimental data, see below). Second, the multi-electron wavepacket in the cation acquires a small correction linear in ϵ , yielding

$$|\Psi^{(D)}(t)\rangle \rightarrow |\Psi^{(D)}(t)\rangle + |\Delta\Psi^{(D)}(t)\rangle = |\Psi^{(D)}(t)\rangle + \epsilon |\delta\Psi^{(D)}(t)\rangle$$

Here $|\delta\Psi^{(D)}(t)\rangle = |\Delta\Psi^{(D)}(t)\rangle/\epsilon$.

Thus, for R and S enantiomers, the harmonic amplitude as a function of ϵ is

$$\begin{aligned} D_{R,S}(N, \epsilon) &= [D_{R,S}(N, \epsilon=0) + \Delta D_{R,S}(N)] \exp\left[-\frac{\epsilon^2}{4\sigma^2}\right] \\ &= [D_{R,S}(N, \epsilon=0) + \epsilon \delta D_{R,S}(N)] \exp\left[-\frac{\epsilon^2}{4\sigma^2}\right] \end{aligned} \quad (4)$$

This expression is completely general and does not rely on equation (3): what it assumes is a linear response in the cation to the fields acting along the minor component of the polarization ellipse.

For a linearly polarized field, $D_{R,S}(N, \epsilon=0) = D_{R,S}^{(0)}(N)$ is not chiral-sensitive (once averaged over a randomly oriented ensemble), $D_S^{(0)}(N) = D_R^{(0)}(N) = D^{(0)}(N)$. The chiral-sensitive component is $\epsilon \delta D_{R,S}(N)$. It corresponds to the recombination of the continuum wavepacket with the chiral-sensitive part of the electronic wavepacket in the cation,

$$\delta D_{R,S}(N) = \langle \delta\Psi_{R,S}^{(D)}(t_N) | \hat{d} | \Psi^{(c)}(t_N) \rangle$$

The chiral-sensitive component has opposite sign for the two enantiomers, so that equation (4) can be rewritten as

$$D_{R,S}(N, \epsilon) = [D^{(0)}(N) \pm \epsilon \delta D_{ch}(N)] \exp\left[-\frac{\epsilon^2}{4\sigma^2}\right]$$

with subscript 'ch' denoting the chiral contribution.

The harmonic yield $Y(N, \epsilon)$ is proportional to the mod-square of this expression, which for a small chiral contribution yields

$$Y_{R,S}(N, \epsilon) = |D^{(0)}(N)|^2 \left[1 \pm 2\epsilon \frac{|\delta D_{ch}(N)|}{|D^{(0)}(N)|} \cos(\Phi_{ch}(N)) \right] \exp\left[-\frac{\epsilon^2}{2\sigma^2}\right]$$

Here Φ_{ch} is the relative phase between the chiral and achiral contributions to the emission amplitude. For a small chiral contribution, this expression can also be written as

$$Y_{R,S}(N, \epsilon) \simeq |D^{(0)}(N)|^2 \exp\left[-\frac{(\epsilon \mp \epsilon_0)^2}{2\sigma^2}\right] \quad (5)$$

where the ellipticity ϵ_0 maximizing the signal is expressed using the amplitude of the chiral-sensitive contribution to the harmonic signal,

$$\frac{\epsilon_0}{\sigma^2} = 2 \frac{|\delta D_{ch}(N)|}{|D^{(0)}(N)|} \cos(\Phi_{ch}) \quad (6)$$

Equation (5) is valid as long as the maximizing ellipticity ϵ_0 is small compared to the width σ of the overall ellipticity dependence, which is the case in all our measurements.

Using equations (5) and (6) the ϵ -weighted chiral signal, $S(N, \epsilon) = (2/\epsilon)(Y_S(N, \epsilon) - Y_R(N, \epsilon))/(Y_S(N, \epsilon) + Y_R(N, \epsilon))$, yields

$$S(N, \epsilon) \simeq 2 \frac{\epsilon_0(N)}{\sigma^2}$$

and

$$S(N, \epsilon) \simeq 4 \frac{|\delta D_{ch}(N)|}{|D^{(0)}(N)|} \cos(\Phi_{ch}(N)) = 2 \frac{\epsilon_0(N)}{\sigma^2}$$

These equations yield two important conclusions. First, the standard measure of the chiral signal, when applied to high-harmonic yield, is proportional to the amplitude $|\delta D_{\text{ch}}(N)| \cos(\Phi_{\text{ch}}(N))$, which is the recombination amplitude of the continuum electron with the chiral-sensitive component of the multi-electron wavepacket in the cation. Second, the ellipticity ϵ_0 , which maximizes the harmonic yield, directly measures the chiral contribution to the recombination amplitude. Because of the $1/\epsilon$ weight, $S(N, \epsilon)$ does not depend on ϵ .

Time-dependent Schrödinger equation (TDSE) simulations. The chiral sensitivity of HHG due to the type-I mechanism was studied by considering a model chiral system and solving the TDSE exactly, and considering the real chiral molecules and performing calculations within the strong-field eikonal-Volkov approximation (SF-EVA; ref. 34, see, for example, refs 26,28,35, for applications to HHG). Here we describe the TDSE approach for the model chiral system. The SF-EVA method used for fenchone and epoxypropane is described in the next section.

Our model chiral system had a single active electron and four nuclei located at $(x_1=0, y_1=0, z_1=0)$, $(x_2=7 \text{ a.u.}, y_2=0, z_2=0)$, $(x_3=0, y_3=4 \text{ a.u.}, z_3=0)$ and $(x_4=0, y_4=0, z_4=10 \text{ a.u.})$, with the effective nuclear charges all equal to 0.5, yielding the ionization potential $I_p = 10.6 \text{ eV}$, similar to that of fenchone.

We solved the TDSE for the frozen nuclei,

$$\left(H - i \frac{\partial}{\partial t}\right) \Psi(\mathbf{r}, t) = \left(-\frac{1}{2} \nabla^2 + V_c(\mathbf{r}) + V_l(\mathbf{r}, t) - i \frac{\partial}{\partial t}\right) \Psi(\mathbf{r}, t) = 0$$

starting in the ground state of the system $\Psi(\mathbf{r}, 0) = \phi_0(\mathbf{r})$. The ground state of our chiral system, ϕ_0 , was obtained by implementing the iterative diagonalization Lanczos method on a Cartesian grid³⁶. The potential V_c includes all electron-nuclei interactions; V_l is the time-dependent electron-field interaction.

In the dipole approximation, the length gauge electron-field interaction is $V_l(\mathbf{r}, t) = \mathbf{r} \cdot \mathbf{E}(t)$, with $\mathbf{E}(t) = E_0(\epsilon \cos(\omega_0 t) \hat{\mathbf{e}}_x + \sin(\omega_0 t) \hat{\mathbf{e}}_z) / \sqrt{1 + \epsilon^2}$. To study the type-I mechanism, we had to go beyond the dipole approximation and include the effect of the magnetic field \mathbf{B} on the continuum electron. The corresponding Hamiltonian is

$$H' = \frac{\mathbf{p}^2}{2} + V_c(\mathbf{r}) + \mathbf{r} \cdot \mathbf{E}(t) - B_z(t) y p_x + B_x(t) y p_z$$

The calculations were performed using the GridTDSE Parallel Fortran 95 code^{37,38} on the 3D Cartesian grid, using the leapfrog propagation method. The calculations were performed for a given orientation j of the model molecule in the lab frame, before orientation averaging.

We considered one full oscillation of the laser field with $\lambda = 800 \text{ nm}$, $I = 10^{14} \text{ W cm}^{-2}$ and $\epsilon = 0.1$, with the main electric field component along the z axis. The z -grid was from -100 to 100 a.u. , whereas the x - and y -grids from -50 to 50 a.u. and -35 to 35 a.u. . The total number of grid points was 89.6×10^6 , the grid step was 0.25 a.u. , and the time step was $\delta t = 1.2 \times 10^{-4} \text{ fs}$. The convergence with respect to all the parameters has been carefully checked. An additional absorbing potential was introduced to avoid artefacts due to reflections from the grid edges, but the grid was large enough for the parameters of the calculation.

Ehrenfest's theorem was used to compute the accelerations of the dipole terms³⁹, $\mathbf{a}_x^{(j,\epsilon)}(t) = (d^2/dt^2) \langle \Psi_{j,\epsilon} | x | \Psi_{j,\epsilon} \rangle$ and $\mathbf{a}_z^{(j,\epsilon)}(t) = (d^2/dt^2) \langle \Psi_{j,\epsilon} | z | \Psi_{j,\epsilon} \rangle$. The HHG yield was computed as the Fourier transform $H_j(\omega, \epsilon) = H_j(n\omega_0, \epsilon) = |\text{FT}(\mathbf{a}_x^{(j,\epsilon)}(t))|^2 + |\text{FT}(\mathbf{a}_z^{(j,\epsilon)}(t))|^2$. The results of our simulations are shown in the Supplementary Information.

Type-I mechanism of cHHG for epoxypropane and fenchone. To study the type-I mechanism in real molecules, we used the strong-field eikonal-Volkov approximation, SF-EVA (ref. 34). Its application to HHG is described in detail in refs 26,28,35,40. The high-harmonic response for a fixed-in-space molecule is^{24,40,41}

$$\mathbf{d}(t_r) = \sum_{t_i} \frac{1}{\sqrt{i}} a_{\text{ion}}(\mathbf{E}(t_i)) a_{\text{prop}}(t_r, t_i) \mathbf{a}_{\text{rec}}(\mathbf{K}(t_r)) \quad (7)$$

Here a_{ion} is the ionization amplitude, a_{prop} is the propagation amplitude, and \mathbf{a}_{rec} is the recombination dipole amplitude vector. The summation is over all stationary ionization times, corresponding to recombination at time t_r . The amplitudes are²⁴

$$a_{\text{ion}} \propto c_{\text{ion}} \left(\frac{\mathbf{E}(t_i)}{E(t_i)} \right) \exp\left(-\frac{1}{3} \frac{(2\text{IP} + K^2(t_i))^{3/2}}{E(t_i)}\right) \quad (8)$$

$$a_{\text{prop}} \propto \left(\frac{2\pi}{t_r - t_i} \right)^{3/2} \exp(i\phi_{\text{st}}) \quad (9)$$

$$\mathbf{a}_{\text{rec}} \propto \langle \phi_d | \mathbf{r} | \mathbf{K}(t_r) \rangle$$

In (8)–(9), IP is the ionization potential, $\mathbf{K}(t)$ is the continuum electron kinetic momentum at time t , and the factor c_{ion} summarizes the orientation dependence of the molecular ionization probability. The specific

definitions of these two quantities will be given below. The phase of the emission ϕ_{st} is given by

$$\phi_{\text{st}} = -\text{IP}(t_r - t_i) - \frac{1}{2} \int_{t_i}^{t_r} K^2(\tau) d\tau$$

ϕ_d is the 1-particle Dyson orbital

$$\langle \phi_d | = \sqrt{N} \langle \Psi_n | \Psi_c \rangle$$

where Ψ_n is the N -electron wavefunction of the neutral species, and Ψ_c is the $(N-1)$ -electron wavefunction of the corresponding cation. Finally, $|\mathbf{K}\rangle$ is the scattering state, corresponding to a plane wave with momentum \mathbf{K} at infinity.

With the magnetic field effects included in the lowest order in $1/c$, the continuum electron kinetic momentum $\mathbf{K}(t)$ is

$$\mathbf{K}(t) = \mathbf{p}_{\text{st}} + \mathbf{A}(t) + \hat{\mathbf{y}} \frac{1}{2c} (2\mathbf{p}_{\text{st}} \cdot \mathbf{A}(t) + A^2(t))$$

where \mathbf{A} is the field vector potential at the origin. Finally, the equations that connect the ionization and recombination times and the drift (canonical) momentum \mathbf{p}_{st} are obtained following the standard sequence of steps^{24,40,42}, the result (to $1/c^2$ accuracy) is^{42,43}

$$0 = \text{IP} + \frac{1}{2} K^2(t_0) \quad (10)$$

$$t_i = \Re(t_0)$$

$$p_{\text{st},x} = \frac{-1}{t_r - t_i} \int_{t_i}^{t_r} A_x(\tau) d\tau \quad (11)$$

$$p_{\text{st},z} = \frac{-1}{t_r - t_i} \int_{t_i}^{t_r} A_z(\tau) d\tau \quad (12)$$

$$p_{\text{st},y} = \frac{1}{c} (p_{\text{st},x}^2 + p_{\text{st},z}^2) - \frac{1}{2c(t_r - t_i)} \int_{t_i}^{t_r} A^2(\tau) d\tau$$

The stationary-phase conditions for the ionization time t_0 of equation (10) and the momentum components within the laser polarization plane $p_{\text{st},x}$, $p_{\text{st},z}$ (11), (12) coincide with the dipole-approximation results. The non-dipole effect is the appearance of the out-of-plane momentum p_y , which makes the continuum trajectory chiral. Its magnitude remains small, $p_{\text{st},y}/p_{\text{st},x} \sim |p|/c$.

As mentioned earlier, the HHG emission from a sample of randomly aligned molecules requires coherent averaging of the radiating dipoles of (7) over the ensemble. If all molecular orientations are equally probable, the average is given in terms of Euler angles (α, β, γ)

$$\mathbf{D}^R = \frac{1}{8\pi^2 \sqrt{i}} a_{\text{prop}}(t_r, t_i) \iiint d\alpha d\beta \sin(\beta) d\gamma \quad (13)$$

$$\{ \mathbb{U}^\dagger \mathbf{a}_{\text{rec}}^R(\mathbb{U} \mathbf{K}(t_r)) a_{\text{ion}}^R(\mathbb{U} \mathbf{E}(t_i)) \}$$

where the summation over different stationary ionization times t_i , separating the trajectories, has been omitted. The propagation amplitude a_{prop} does not depend on the molecular orientation (the dependence is encoded into ionization and recombination), and can be moved outside of the integral. The R superscripts on $\mathbf{a}_{\text{rec}}^R$ and a_{ion}^R emphasize that the matrix elements are for the 'normal' molecular isomer.

The matrix $\mathbb{U} = \mathbb{U}(\alpha, \beta, \gamma)$ describes transformation of a vector from the laboratory frame into the molecular frame. Its transpose \mathbb{U}^\dagger defines the inverse transformation into the laboratory frame. $\mathbb{U} \mathbf{E}(t_i)$ is the instantaneous electric field in the molecular frame at the time of ionization t_i . Its value determines the molecular ionization amplitude. Similarly, the laboratory-frame kinetic momentum at recollision $\mathbf{K}(t_r)$ determines the molecular-frame recombination dipole amplitude $\mathbf{a}_{\text{rec}}(\mathbb{U} \mathbf{K}(t_r))$. The amplitude is then transformed back to the laboratory frame for coherent averaging.

To calculate the HHG response of a randomly oriented ensemble of S -enantiomers it is convenient to use the plane of laser polarization σ_{pol} as the reflection plane. Applying the reflection operator $\hat{\sigma}_{\text{pol}}$ to (13) is equivalent to reflecting the laser fields and continuum-state momentum in the arguments of the matrix elements, so that

$$\mathbf{D}^S = \frac{1}{8\pi^2 \sqrt{i}} a_{\text{prop}}(t_r, t_i) \iiint d\alpha d\beta \sin(\beta) d\gamma$$

$$\{ \mathbb{U}^\dagger \mathbf{a}_{\text{rec}}^S(\mathbb{U} \mathbf{K}(t_r)) a_{\text{ion}}^S(\mathbb{U} \mathbf{E}(t_i)) \}$$

$$= \frac{1}{8\pi^2 \sqrt{i}} a_{\text{prop}}(t_r, t_i) \iiint d\alpha d\beta \sin(\beta) d\gamma$$

$$\{ \hat{\sigma}_{\text{pol}} \mathbb{U}^\dagger \mathbf{a}_{\text{rec}}^R(\mathbb{U} \hat{\sigma}_{\text{pol}} \mathbf{K}(t_r)) a_{\text{ion}}^R(\mathbb{U} \mathbf{E}(t_i)) \}$$

where we have used $\hat{\sigma}_{\text{pol}}\mathbf{E}(t_i) = \mathbf{E}(t_i)$ so that no reflection operation appears in the a_{ion}^R amplitude.

Type-II mechanism of cHHG in strong mid-IR fields. To study the Type-II mechanism, we used the approach described in ref. 40, validated in our previous work^{26,28,35}. Let the two ionic states, labelled X and A, participate in the harmonic generation process. Compared to the single-channel HHG described by equation (7), the time-dependent dipole becomes⁴⁰

$$\mathbf{d}(t_r) = \mathbf{d}_{\text{XX}}(t_r) + \mathbf{d}_{\text{AA}}(t_r) + \mathbf{d}_{\text{XA}}(t_r) + \mathbf{d}_{\text{AX}}(t_r)$$

Here \mathbf{d}_{IF} describes the harmonic emission process where ionization leaves the ion in the state I but recombination occurs with the ion in the state F. The state F can be different from I owing to the laser-induced transitions in the ion, which can occur between ionization and recombination. These transitions have been modelled by solving the TDSE in the basis of essential electronic states using appropriate quantum chemical input for electric and magnetic coupling dipoles (see Supplementary Information). Each dipole \mathbf{d}_{IF} also includes ionization and recombination amplitudes. We used TD-RIS (ref. 44) for the analysis of the angular-dependent ionization rates and EVA (eikonal-Volkov)^{26,28,34,35} calculations for the analysis of the recombination dipoles.

References

- Budil, K. S., Salières, P., Perry, M. D. & L'Huillier, A. Influence of ellipticity on harmonic generation. *Phys. Rev. A* **48**, R3437–R3440 (1993).
- Sukiasyan, S., Patchkovskii, S., Smirnova, O., Brabec, T. & Ivanov, M. Exchange and polarization effect in high-order harmonic imaging of molecular structures. *Phys. Rev. A* **82**, 043414 (2010).
- Patchkovskii, S., Zhao, Z., Brabec, T. & Villeneuve, D. M. High harmonic generation and molecular orbital tomography in multielectron systems. *J. Comput. Phys.* **126**, 114306 (2007).
- Smirnova, O., Spanner, M. & Ivanov, M. Analytical solutions for strong field-driven atomic and molecular one- and two-electron continua and applications to strong-field problems. *Phys. Rev. A* **77**, 033407 (2008).
- Smirnova, O. *et al.* Attosecond circular dichroism spectroscopy of polyatomic molecules. *Phys. Rev. Lett.* **102**, 063601 (2009).
- Huang, S. W. & Carrington, T. A comparison of filter diagonalisation methods with the Lanczos method for calculating vibrational energy levels. *Chem. Phys. Lett.* **312**, 311–318 (1999).
- Suarez, J., Farantos, S. C., Stamatiadis, S. & Lathouwers, L. A method for solving the molecular Schrödinger equation in cartesian coordinates via angular momentum projection operators. *Comput. Phys. Commun.* **180**, 2025–2033 (2009).
- Kosloff, R. *Dynamics of Molecules and Chemical Reactions* 185–230 (CRC Press, 1996).
- Burnett, K., Reed, V. C., Cooper, J. & Knight, P. L. Calculation of the background emitted during high-harmonic generation. *Phys. Rev. A* **45**, 3347–3349 (1992).
- Smirnova, O. & Ivanov, M. *Attosecond and XUV Physics: Ultrafast Dynamics and Spectroscopy*, Ch. 7 201–256 (Wiley-VCH, 2014).
- Lewenstein, M., Balcou, P., Ivanov, M. Y., L'Huillier, A. & Corkum, P. B. Theory of high-harmonic generation by low-frequency laser fields. *Phys. Rev. A* **49**, 2117–2132 (1994).
- Shafir, D. *et al.* Resolving the time when an electron exits a tunneling barrier. *Nature* **485**, 343–346 (2012).
- Chirilă, C. C., Kylstra, N. J., Potvliege, R. M. & Joachain, C. J. Nondipole effects in photon emission by laser-driven ions. *Phys. Rev. A* **66**, 063411 (2002).
- Spanner, M. & Patchkovskii, S. One-electron ionization of multielectron systems in strong nonresonant laser fields. *Phys. Rev. A* **80**, 063411 (2009).